Transverse laser cooling induced through dispersion at an rf cavity

Hiromi Okamoto*,†
Lawrence Berkeley Laboratory, 1 Cyclotron Road, Berkeley, California 94720
(Received 11 May 1994; revised manuscript received 28 July 1994)

We propose a possible scheme to realize three-dimensional laser cooling of stored and circulating ion beams in a storage ring. The idea is based on creating a linear synchrobetatron coupling such that the longitudinal laser cooling effect can be extended to transverse degrees of freedom through the coupling. The idea of indirect transverse laser cooling was recently studied, employing a so-called *coupling cavity* as a source of the forced coupling. In the present paper, we theoretically explore the possibility of using natural dispersion of a ring as an alternative coupling source, setting an *ordinary* rf cavity at a position with nonzero dispersion. It is found that the effect of the dispersion-induced coupling is essentially equivalent to that of the coupling cavity, and that the coupling can be considerably enhanced under resonance conditions. The cooling rates of longitudinal and transverse modes are evaluated. An approximate formula is derived to estimate an optimum value of dispersion at the cavity location. The validity of the present theoretical predictions is confirmed by tracking simulations that demonstrate effective transverse laser cooling.

PACS number(s): 29.20.Dh, 29.27.Fh

I. INTRODUCTION

To date, several techniques have been available to cool down the temperatures of stored and circulating beams of particles. Electron cooling [1] and stochastic cooling [2] are the well-known and well-established methods which have been widely employed to provide stored beams with very small emittances. These two techniques work fairly effectively in all three degrees of freedom, reducing beam temperatures typically to the 10^1-10^2-K range. On the other hand, there exists a third promising method known as laser cooling [3], which is the result of velocity-selective photon-momentum transfer from a laser beam to a moving atom or ion. The effectiveness of this mechanism has already been experimentally demonstrated [4], achieving longitudinal temperatures in the mK range, the lowest ever reported, with a stored beam of 100-keV $^7Li^+$ ions [5]. The laser cooling of a circulating beam, however, is limited to longitudinal motion. No effective damping of transverse emittances has so far been accomplished, in contrast with its successful operation upon longitudinal momentum spread. In fact, in the above-mentioned experiment, the transverse temperature of the laser-cooled $^7Li^+$ beam was about 10^6 times higher than the longitudinal temperature.

Recently, a method has been proposed to realize *three-dimensional* laser cooling in a storage ring [6]. The idea is based on forcibly developing a synchrobetatron coupling; that is, somehow opening up a path which connects the longitudinal degree of freedom directly with the transverse ones such that the longitudinal damping action due to the laser cooling mechanism can be transferred into transverse directions. For this purpose, in the previous work, a so-called *coupling cavity* excited in the TM_{210} mode was introduced. The longitudinal electric field of the mode has a linear transverse-coordinate dependence which makes it possible to obtain an efficient coupling between longitudinal and transverse motions. It has been found that, to enhance the coupling, it was necessary to drive the operating point of a storage ring onto a difference resonance. This idea, however, involves a difficulty in designing the coupling cavity itself when the energy of laser-cooled ions is very small. For a low-energy beam, a rather small operating frequency must be chosen because of some beam-dynamical reasons, but the cavity dimension may then become impracticably large due to its operating mode. The difficulty can be overcome by using a specially designed cavity which might be a reentrant type with lumped impedances supplied by a coil.

In this paper, we explore an alternative scheme for three-dimensional laser cooling. The basic idea is the same as before, that is, developing a forced coupling between longitudinal and transverse motion under a resonance condition, but here the natural dispersion of a ring is considered as the coupling source. It is, in principle, always possible to induce a synchrobetatron coupling by setting some time-dependent or horizontal-coordinate-dependent potential at a position with nonzero dispersion. An rf cavity is again utilized for this purpose. The operating mode, however, is not a special one like TM_{210} but a coaxial or TM_{010} mode which has long been employed for ordinary accelerating cavities. Therefore, we do not have to worry about the cavity size problem even if the required rf frequency is low. The use of a coaxial-mode structure allows us to design a cavity of modest dimension.

*Permanent address: Accelerator Laboratory, Institute for Chemical Research, Kyoto University, Gokanoshou, Uji, Kyoto 611, Japan.
†Present address: CERN/SL Division, CH-1211 Geneva 23, Switzerland.

Compared to the idea of the coupling cavity, the significance of the present scheme is its simplicity. Clearly, there is no component we must newly devise, while, in the previous idea, the design of the coupling cavity is not so straightforward and is left for future work. All we need to do under the present scheme is to design a proper lattice satisfying the theoretically required conditions, and then to install an ordinary rf cavity at a position having a finite dispersion. Provided that the existing rings employed for laser cooling experiments, i.e., TSR in Germany [4] and ASTRID in Denmark [5,7], are sufficiently tunable and have a free section with nonzero dispersion, it is only necessary to set an additional cavity in the section or, simply, to bring the existing accelerating cavity to that section. As demonstrated below, the magnitude of dispersion at the cavity position is not essentially important, because cooling rates of longitudinal and transverse motions can be controlled with the strength of a skew quadrupole introduced to give a horizontal-vertical coupling.

In principle, the dispersive-coupling scheme enables us to cool transverse beam temperatures down to the same level as longitudinal temperature. In the ASTRID ring, a longitudinal temperature of 1 mK has already been achieved, so we can reasonably anticipate the same order of temperatures simultaneously in both horizontal and vertical directions. If this kind of ultracold beam becomes available, we might then consider some important applications of such a beam. First, analogous to electron cooling, the laser-cooled beam could be used to cool another beam to an extremely low temperature. Second, the achievable level of beam temperature should theoretically be sufficient to observe beam crystallization [8].

The paper is organized as follows. In Sec. II, we give the linearized equations of motion derived from the Hamiltonian including the potentials of an rf cavity and a pure skew quadrupole. Then a simple model is presented to incorporate the laser-cooling effect. The coupling caused by the skew quadrupole is investigated in Sec. III, switching off the rf cavity. In Sec. IV, we first confirm the effectiveness of the longitudinal-horizontal coupling induced through dispersion at the rf cavity, leading to results similar to those obtained in the previous work [6]. The three-dimensional effect is then studied, and an optimum operating point is theoretically predicted. In Sec. V, tracking results are given, demonstrating the validity of the present theoretical predictions. The effect of finite dispersion at the skew-quadrupole position as well as that of the finite dispersion derivative at the cavity are briefly discussed in Sec. VI. We then summarize the main results of the paper in Sec. VII.

II. EQUATIONS OF MOTION

A. Linearized equations without laser cooling effect

Since a single rf cavity and a single skew quadrupole turn out to be sufficient to achieve our final goal, we simply set $N_b=1=N_q$ in the Hamiltonian (A7) given in Appendix A to obtain

$$H_4=\tfrac{1}{2}(\hat{p}_x^2+\hat{p}_y^2)+\tfrac{1}{2}[K_x(s)\hat{x}^2+K_y(s)\hat{y}^2]-\left[\frac{h}{R}\right]^2\frac{\xi_0\hat{W}^2}{2}+\hat{y}\left[\hat{x}-\frac{h\eta}{R}\hat{W}\right]\frac{\Gamma_q}{R}\delta_p(s-s_q)-\frac{qV_b}{p_0\omega}\sin\left[\hat{\psi}-\frac{h}{R}(\eta\hat{p}_x-\eta'\hat{x})+\psi_b\right]\delta_p(s-s_b)\ , \tag{2.1}$$

where the additional phase variable has been defined as $\hat{\psi}\equiv\hat{\phi}-\psi_b$ with the synchronous phase ψ_b. The ions susceptible to laser cooling are heavy particles for which the synchrotron radiation loss is negligible, so it is unnecessary to accelerate to compensate for energy loss. The rf cavity is then introduced here for two reasons: creating a longitudinal-horizontal coupling, and forcing particles to execute synchrotron oscillations as an origin of the resonance needed to enhance the coupling [9]. In addition, the energy of stored heavy ions is, in general, below transition, i.e., $\xi_0<0$, and ψ_b must then be positive in the definition adopted here. Accordingly, to make the rf bucket as large as possible, we choose the synchronous phase $\psi_b=\pi/2$ in the following. We also assume throughout this paper, in the numerical work, that $\xi_0=-0.947$ and $2\pi R=40$ m, corresponding to the ASTRID ring parameters.

Scaling the canonical variable and changing the independent variable to $\theta=s/R$, Eq. (2.1) results in the Hamiltonian

$$H=\tfrac{1}{2}(p_x^2+\nu_x^2x^2)+\tfrac{1}{2}(p_y^2+\nu_y^2y^2)-\frac{\xi_0W^2}{2}+\Gamma_q(x-\zeta_qW)y\delta_p(\theta-\theta_q)-\frac{hqV_b}{p_0\beta_0c}\cos(\psi+\dot{\zeta}_bx-\zeta_bp_x)\delta_p(\theta-\theta_b)\ , \tag{2.2}$$

where the dot denotes differentiation with respect to θ, $\zeta_q\equiv\eta(\theta=\theta_q)/R$, $\zeta_b\equiv\eta(\theta=\theta_b)/R$, $\dot{\zeta}_b\equiv\dot{\eta}(\theta=\theta_b)/R$, and the hats on the variables have been dropped. Here the betatron motions have been smoothed introducing the one-turn tunes, ν_x in the horizontal direction and ν_y in the vertical direction. Note that all the canonical variables have now become dimensionless due to the scaling performed. Neglecting the higher order terms in Eq. (2.2), we reach the linearized Hamiltonian equations of motion

$$\dot{x}=p_x+\frac{2\pi\zeta_b\bar{\nu}_L^2}{\xi_0}(\psi+\dot{\zeta}_bx-\zeta_bp_x)\delta_p(\theta-\theta_b)\ , \tag{2.3}$$

$$\dot{p}_x=-\nu_x^2x-\Gamma_qy\delta_p(\theta-\theta_q)+\frac{2\pi\dot{\zeta}_b\bar{\nu}_L^2}{\xi_0}(\psi+\dot{\zeta}_bx-\zeta_bp_x)\delta_p(\theta-\theta_b)\ , \tag{2.4}$$

$$\dot{y}=p_y\ , \tag{2.5}$$

$$\dot{p}_y=-\nu_y^2y-\Gamma_q(x-\zeta_qW)\delta_p(\theta-\theta_q)\ , \tag{2.6}$$

$$\dot{\psi}=-\xi_0W-\Gamma_q\zeta_qy\delta_p(\theta-\theta_q)\ , \tag{2.7}$$

$$\dot{W}=\frac{2\pi\bar{\nu}_L^2}{\xi_0}(\psi+\dot{\zeta}_b x-\zeta_b p_x)\delta_p(\theta-\theta_b)\ , \tag{2.8}$$

where $\bar{\nu}_L^2\equiv hq|\xi_0|V_b/2\pi p_0\beta_0 c$ corresponds to the one-turn averaged tune of the synchrotron motion. A more accurate value of the longitudinal tune ν_L is evaluated under a thin lens approximation, and can be related to the averaged tune as

$$\cos(2\pi\nu_L)=1-2\pi^2\bar{\nu}_L^2\ . \tag{2.9}$$

Specifically, $\bar{\nu}_L$ gives roughly the same value as ν_L when the tune is small.

Provided that the phase spread of a stored beam is sufficiently small, we are well justified in starting with the linearized equations given above, since the terms $\dot{\zeta}_b x$ and $\zeta_b p_x$ mostly take quite small values in our applications [10]. Although the laser cooling mechanism itself does not require us to bunch an initial continuous beam, it may be better to bunch it first to get into the simple linear regime. For this purpose, the rf cavity originally intended for generating a synchrobetatron coupling can be employed without any severe nonlinear effect setting in. In fact, an rf cavity sitting at a position where $\eta_b=2.72$ m has been used in the ASTRID ring to bunch a beam of 100-keV $^{24}Mg^+$ ions [11]. Further, tracking simulations indicate that an initial phase spread of even more than 100° is acceptable, so the beam is not necessarily *well bunched.* We recall this problem in Sec. V, linking it to beam-size growths due to an initial emittance unbalance.

B. Model

We are now in a position to incorporate the effect of laser cooling into the equations of motion. Because of Liouville's theorem, damping of phase-space volume, i.e., cooling, is not possible as far as the given motion is derivable from a Hamiltonian. We must, therefore, take into account something additional which enables us to have a dissipative process like cooling. In our model, the cooling effect is expressed as a simple frictional force. Noting the fact that laser cooling operates only in the longitudinal direction, the damping term is added to Eq. (2.8), yielding

$$\dot{W}=\frac{2\pi\bar{\nu}_L^2}{\xi_0}(\psi+\dot{\zeta}_b x-\zeta_b p_x)\delta_p(\theta-\theta_b)-\Lambda W\varepsilon(\theta_{\rm ent},\theta_{\rm ext})\ , \tag{2.10}$$

where $\theta_{\rm ent}$ and $\theta_{\rm ext}$ represent the θ coordinates of the entrance and exit of the cooling section respectively, and $\varepsilon(\theta_{\rm ent},\theta_{\rm ext})$ is the periodic step function defined by

$$\varepsilon(\theta_{\rm ent},\theta_{\rm ext})=\begin{cases}1 & \text{for } \theta_{\rm ent}\le\theta\le\theta_{\rm ext}\\ 0 & \text{for other regions.}\end{cases}$$

To obtain a damping motion, the constant Λ must be always positive. The value of Λ can be determined by comparing simulation results with actual experimental data.

Let us construct the transfer matrix of a laser cooling section. Equation (2.10) together with Eq. (2.7) results in either $\ddot{\psi}+\Lambda\dot{\psi}=0$ or $\ddot{W}+\Lambda\dot{W}=0$ for $\theta_{\rm ent}\le\theta\le\theta_{\rm ext}$. Clearly, these equations have a damping solution when $\Lambda>0$. Since the betatron oscillations are completely decoupled in the section, the damping matrix can be written as

$$\mathbf{M}_D(\theta_D)=\begin{bmatrix}\cos(\nu_x\theta_D) & \sin(\nu_x\theta_D)/\nu_x & 0 & 0 & 0\\ -\nu_x\sin(\nu_x\theta_D) & \cos(\nu_x\theta_D) & & & \\ 0 & 0 & \cos(\nu_y\theta_D) & \sin(\nu_y\theta_D)/\nu_y & 0\\ & & -\nu_y\sin(\nu_y\theta_D) & \cos(\nu_y\theta_D) & \\ 0 & 0 & & 1 & [e^{-\Lambda\theta_D}-1]\xi_0/\Lambda\\ & & & 0 & e^{-\Lambda\theta_D}\end{bmatrix}, \tag{2.11}$$

where $\theta_D=\theta_{\rm ext}-\theta_{\rm ent}$. This matrix is, of course, not symplectic.

Equations (2.3)–(2.8) indicate that a coupling between the longitudinal and horizontal motions can be induced through the dispersion ζ_b and/or its derivative $\dot{\zeta}_b$ at the cavity position. Specifically, we do not have to make ζ_b and $\dot{\zeta}_b$ nonzero simultaneously. Thus we simply assume $\dot{\zeta}_b=0$ in the following discussions. From a practical point of view, this simplification is quite reasonable, because most storage rings have straight sections with a flat dispersion, and that is the region where rf cavities are usually installed. In fact, the two storage rings, ASTRID and TSR, belong to the case. Moreover, if a finite value of $\dot{\zeta}_b$ is employed, the cavity must then be set at the exact design position. The use of a flat dispersion allows us to avoid this extra effort.

Finally, for later reference, we give the approximate equations of the synchrobetatron motion studied here, averaging the damping term and longitudinal kick at the cavity over one turn. Under the assumption $\dot{\zeta}_b=0$, Eqs. (2.3)–(2.7) and (2.10) lead to

$$\ddot{x}+\nu_x^2\left[1-\frac{(\zeta_b\nu_L)^2}{\xi_0}\right]x=-\zeta_b\nu_L^2 W-\left[1-\frac{(\zeta_b\nu_L)^2}{\xi_0}\left[1-\frac{\zeta_q}{\zeta_b}\right]\right]\times\Gamma_q y\delta_p(\theta-\theta_q)\ , \tag{2.12}$$

$$\ddot{y}+\nu_y^2 y=-(x-\zeta_q W)\Gamma_q\delta_p(\theta-\theta_q)\ , \tag{2.13}$$

$$\ddot{W}+\Lambda_{\rm av}\dot{W}+\nu_L^2 W = \frac{\zeta_b \nu_L^2}{\xi_0}\left[\nu_x^2 x+\left[1-\frac{\zeta_q}{\zeta_b}\right]\Gamma_q y \delta_p(\theta-\theta_q)\right], \quad (2.14)$$

where $\Lambda_{\rm av}$ denotes the averaged damping constant. Note that we have replaced $\bar{\nu}_L$ by ν_L to reduce the discrepancy between the real and averaged synchrotron frequencies.

III. COUPLING THROUGH SKEW QUADRUPOLE

It is clear from the equations of motion that, even if the rf cavity is switched off, we still have synchrobetatron coupling, provided $\zeta_q \neq 0$. In this section, we briefly discuss the effect, checking whether the coupling caused by a skew quadrupole can be helpful to achieve transverse laser cooling. Without any averaging procedure, the equations of motion are written as

$$\ddot{x}+\nu_x^2 x=-\Gamma_q y \delta_p(\theta-\theta_q), \quad (3.1)$$

$$\ddot{y}+\nu_y^2 y=-\Gamma_q (x-\zeta_q W)\delta_p(\theta-\theta_q), \quad (3.2)$$

$$\dot{W}+\Lambda W \varepsilon(\theta_{\rm ent},\theta_{\rm ext})=0. \quad (3.3)$$

Equation (3.3) can be solved readily, leading to a damping solution independent of any transverse parameters. Inversely speaking, this suggests that the betatron motions are not affected by the longitudinal motion and, therefore, we will observe no cooling in the transverse directions. In fact, if the longitudinal damping motion could induce a transverse damping effect through the coupling terms, the longitudinal damping rate must then be influenced by some transverse parameters.

This observation can be proven by evaluating the eigenvalues of the coupled motion. Applying, for simplicity, a thin lens approximation to the damping matrix in Eq. (2.11), and then calculating the one-turn matrix $\mathbf{M}_1$, we find, from the characteristic equation $\det(\mathbf{M}_1-\lambda \mathbf{I})=0$,

$$(\lambda-1)(\lambda-e^{-\Lambda_D})f(\lambda)=0, \quad (3.4)$$

where $\Lambda_D \equiv \Lambda \theta_D$, and $f(\lambda)$ is a fourth-order algebraic equation involving neither ζ_q nor Λ. While the root $\lambda=e^{-\Lambda_D}$ obviously corresponds to longitudinal mode, the cooling rates of transverse modes are evaluated from the equation $f(\lambda)=0$ whose roots are totally independent of the parameter Λ characterizing damping motion. It can therefore be concluded that transverse damping is not achievable by means of the coupling originating from the skew quadrupole potential.

IV. THREE-DIMENSIONAL COOLING SCHEME

We found in Sec. III that the dispersion ζ_q cannot be a source for transverse momentum cooling. The skew quadrupole, therefore, is introduced only for the purpose of coupling the horizontal motion to the vertical motion. Thus, for simplicity, we set $\zeta_q=0$ in this section. The effect of ζ_q on cooling rates is briefly discussed in Sec. VI, showing that a finite ζ_q causes no remarkable change to the results presented below.

A. Longitudinal-horizontal coupling

Let us now turn on the rf cavity. Unless there exist vertical bending magnets, dispersion-induced coupling occurs only between the longitudinal and horizontal directions. Since the skew quadrupole coupling has turned out to be useless in obtaining transverse cooling effect, the most important key is whether or not the coupling generated by the cavity dispersion ζ_b can provide sufficiently high cooling rates in the longitudinal and horizontal directions simultaneously. Thus we first try to investigate these two motions, neglecting the vertical betatron oscillation.

From Eqs. (2.12) and (2.14), the starting equations read

$$\ddot{x}+\nu_x^2\left[1-\frac{(\zeta_b \nu_L)^2}{\xi_0}\right]x=-\zeta_b \nu_L^2 W, \quad (4.1)$$

$$\ddot{W}+\Lambda_{\rm av}\dot{W}+\nu_L^2 W=\frac{\zeta_b(\nu_x \nu_L)^2}{\xi_0}x. \quad (4.2)$$

These equations are essentially equivalent to those discussed in Ref. [6], while the kick force at the cavity here has been averaged over one turn. Similar damping properties can then be expected. Following the results of the previous work, the transverse-emittance damping induced through the dispersive coupling should be most enhanced under the condition of a difference resonance

$$\nu_x\left[1-\frac{(\zeta_b \nu_L)^2}{\xi_0}\right]^{1/2}-\nu_L=\text{integer}. \quad (4.3)$$

Noting that $(\zeta_b \nu_L)^2/|\xi_0| \ll 1$, Eq. (4.3) can be simplified, to a good approximation, as $\nu_x-\nu_L=$integer.

In our case, the best way to evaluate the damping rates is to use the matrix method. Because the kick force at the cavity is linearized here, we can easily construct the corresponding transfer matrix $\mathbf{M}_b$ as given in Appendix B. Using $\mathbf{M}_b$ and the drift matrix $\mathbf{M}_0$ together with the damping matrix in Eq. (2.11), a one-turn matrix can be represented as

$$\mathbf{M}_2 \equiv \mathbf{M}_0(\theta_2)\mathbf{M}_b\mathbf{M}_0(\theta_1)\mathbf{M}_D(\theta_D), \quad (4.4)$$

where, setting the origin of the θ coordinate at the center of the cooling section, θ_1 and θ_2 are defined by $\theta_1=\theta_b-\theta_D/2$ and $\theta_2=2\pi-(\theta_1+\theta_D)$. Neglecting the vertical motion, which is decoupled right now, the equation $\det(\mathbf{M}_2-\lambda \mathbf{I})=0$ yields the dispersion relation

$$\left[\lambda+\frac{1}{\lambda}-2\cos\mu_x\right]\left[\lambda+\frac{e^{-\Lambda_D}}{\lambda}-2\cos\mu_L+(1-e^{-\Lambda_D})(1-2\pi\bar{\nu}_L^2\theta_1)\right]-\frac{2\pi\nu_x\bar{\nu}_L^2\zeta_b^2}{\xi_0}\left[1-\frac{1}{\lambda}\right](\lambda-e^{-\Lambda_D})\sin\mu_x=0, \quad (4.5)$$

where $\mu_x = 2\pi\nu_x$, $\mu_L = 2\pi\nu_L$, and the thin lens approximation has again been applied to the damping matrix. The damping rates numerically evaluated from the matrix $\mathbf{M}_2$ are shown in Fig. 1. Here η_b represents dispersion at the rf cavity, i.e., $\eta_b \equiv \eta(\theta = \theta_b)$, and ν is the eigentune satisfying the relation $\lambda = e^{i2\pi\nu}$. The behavior of $\mathrm{Im}(\nu)$ as a function of the dispersion η_b is quite similar to the previous results in Ref. [6], where $\mathrm{Im}(\nu)$ has been plotted as a function of the field strength of the coupling cavity. As mentioned above, the most effective cooling situation, where the horizontal damping rate becomes roughly equal to the longitudinal damping rate, is provided when the operating point is on resonance. Obviously, Fig. 1(c) is the case. We see that, except for the region $\eta_b \leq 0.25$ m, both damping rates stay close to each other around a constant level.

Considering practical applications, we are interested in the smaller ζ_b region. We then approximately solve Eq. (4.5), employing perturbation analysis with respect to ζ_b^2. Assuming the resonance condition in Eq. (4.3) and again writing $\lambda = e^{i2\pi\nu}$, the imaginary parts of the first-order solutions to Eq. (4.5) can be given by

$$\mathrm{Im}(\nu_1) \approx \frac{\nu_x \bar{\nu}_L^2 \zeta_b^2}{2|\xi_0|} \left[\frac{1}{1-e^{-\Lambda_D}} - \frac{\theta_1}{2\pi} \right] \times \frac{\sin\mu_0}{1-(1-\cos\mu_0)\dfrac{\theta_1}{\pi}\left[1-\dfrac{\theta_1}{2\pi}\right]} , \tag{4.6}$$

$$\mathrm{Im}(\nu_2) \approx \frac{\Lambda_D}{4\pi} - \mathrm{Im}(\nu_1) , \tag{4.7}$$

where, in order to let the tunes satisfy the simplified resonance condition $\nu_x - \nu_L = \text{integer}$, we have set $\mu_x = \mu_0$ and $\mu_L = \mu_0 - 2n\pi$ (n = integer). Here ν_1 denotes the eigentune of the horizontal mode, while ν_2 corresponds to the longitudinal mode.

Some examples of $\mathrm{Im}(\nu)$ under the resonance condition are illustrated in Fig. 2. The dotted curves are obtained from Eqs. (4.6) and (4.7), yielding good agreements in the small-η_b region. Analogous to the results in Ref. [6], the damping rates of both modes are rapidly saturated at the level $\Lambda_D/8\pi$, which is exactly half the longitudinal damping rate without the coupling. Further, unless the dispersion η_b is too large, all damping rates remain positive and, accordingly, we can always more or less, observe a cooling effect in both directions. Of particular importance is the minimum dispersion value η_m desirable to achieve the damping rates close to the saturation level. η_m is readily estimated by equating Eqs. (4.6) and (4.7), resulting in

$$\eta_m^2 \approx \frac{|\xi_0| R^2}{4\pi\nu_x \bar{\nu}_L^2} \frac{\Lambda_D}{\Lambda_D^{-1} - (\theta_1/2\pi)} \times \frac{1-(1-\cos\mu_0)\dfrac{\theta_1}{\pi}\left[1-\dfrac{\theta_1}{2\pi}\right]}{\sin\mu_0} , \tag{4.8}$$

where we have used the approximation $e^{-\Lambda_D} \approx 1 - \Lambda_D$. η_m gives an approximate value of the minimum dispersion at the cavity required for efficient horizontal laser cooling.

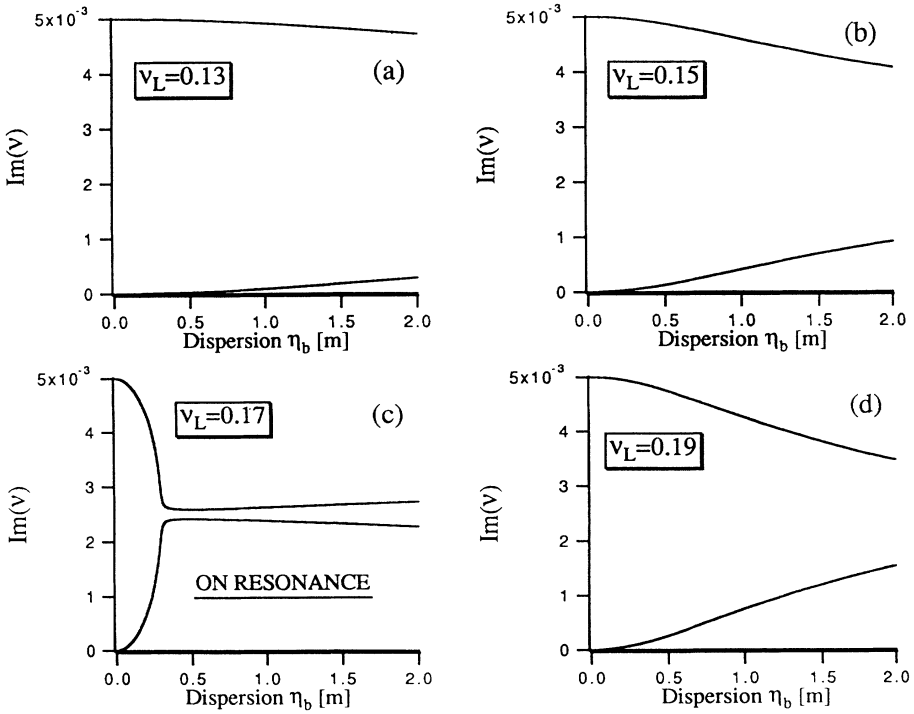

FIG. 1. Imaginary part of the eigentunes describing longitudinal and transverse motions as a function of the dispersion η_b at the rf cavity position. The horizontal tune ν_x is chosen to be $\nu_x = 2.17$ in all cases. The cavity is set at the location opposite to the laser damping section, which has the cooling rate $\Lambda_D/2\pi = 0.01$. In all figures presented in this paper, we use the slip factor $\xi_0 = -0.947$, roughly corresponding to the recent ASTRID experiments for 100-keV $^{24}Mg^+$ ions. In addition, we assume the circumference of the storage ring to be 40 m, the same as in the ASTRID ring.

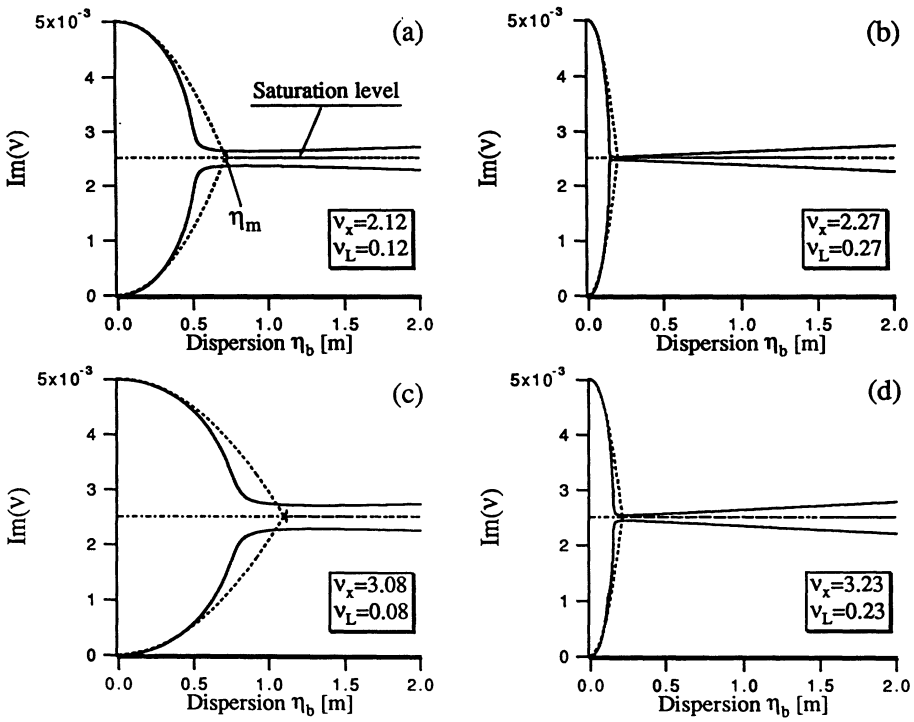

FIG. 2. The same as Fig. 1, but now the tunes are chosen in each case such that the resonance condition $\nu_x-\nu_L$ =integer is satisfied. The solid curves are obtained from solving the 4×4 determinant, while the dotted curves result from Eqs. (4.6) and (4.7).

Equation (4.8) also allows us to predict the preferable position for installing the cavity. The value of θ_1 minimizing η_m is evaluated as

$$\frac{\theta_m}{2\pi}=\frac{1}{\Lambda_D}\left\{1-\left[1-\Lambda_D+\left[\frac{\Lambda_D}{2}\operatorname{cosec}\frac{\mu_0}{2}\right]^2\right]^{1/2}\right\} . \quad (4.9)$$

Equation (4.9) implies that θ_m always takes a value close to π except for the region $\cos\mu_0\approx 1$, because we usually have $\Lambda_D \ll 1$. Thus, to make η_m smallest, the cavity should be set at the position opposite to the laser-cooling section.

B. Three-dimensional laser cooling

We now proceed to three-dimensional analysis. In order to evaluate the damping rates of the three modes, we first try to obtain a dispersion relation based on the general 6×6 matrices given in Appendix B and Eq. (2.11). Since the damping rates are not so sensitive to the location of the skew quadrupole having a modest value of Γ_q, we simply multiply $\mathbf{M}_2$ by $\mathbf{M}_q$ to introduce the one-turn matrix

$$\mathbf{M}_3=\mathbf{M}_q\mathbf{M}_2 . \quad (4.10)$$

Taking $\det(\mathbf{M}_3-\lambda\mathbf{I})=0$ yields, after considerable algebra, the dispersion relation

$$\left[\lambda+\frac{e^{-\Lambda_D}}{\lambda}-2\cos\mu_L+(1-e^{-\Lambda_D})(1-2\pi\bar{\nu}_L^2\theta_1)\right]$$
$$\times\left[\left[\lambda+\frac{1}{\lambda}-2\cos\mu_x\right]\left[\lambda+\frac{1}{\lambda}-2\cos\mu_y\right]-\frac{\Gamma_q^2}{\nu_x\nu_y}\sin\mu_x\sin\mu_y\right]-\frac{2\pi\nu_x\bar{\nu}_L^2\xi_b^2}{\xi_0}\left[1-\frac{1}{\lambda}\right](\lambda-e^{-\Lambda_D})$$
$$\times\left[\left[\lambda+\frac{1}{\lambda}-2\cos\mu_y\right]\sin\mu_x-\frac{\Gamma_q^2\cos(\nu_x\theta_1)\cos(\nu_x\theta_2)}{\nu_x\nu_y}\sin\mu_y\right]=0 , \quad (4.11)$$

where $\mu_y=2\pi\nu_y$, and we have used the thin $\mathbf{M}_D$. Without the quadrupole coupling, i.e., $\Gamma_q=0$, the vertical mode is, of course, decoupled, and Eq. (4.11) is reduced to Eq. (4.5). Similarly to Sec. IV A, the damping rates of all modes can be found by evaluating the eigenvalue λ. Figure 3 shows some typical features of the damping-rate curves plotted as a function of the dispersion η_b.

As pointed out already, the resonance condition in Eq. (4.3) is required to increase the horizontal damping rate. Here, in addition to the longitudinal-horizontal coupling, we must consider a coupling between the two transverse motions. Comparing the coupling terms in Eqs. (4.1) and

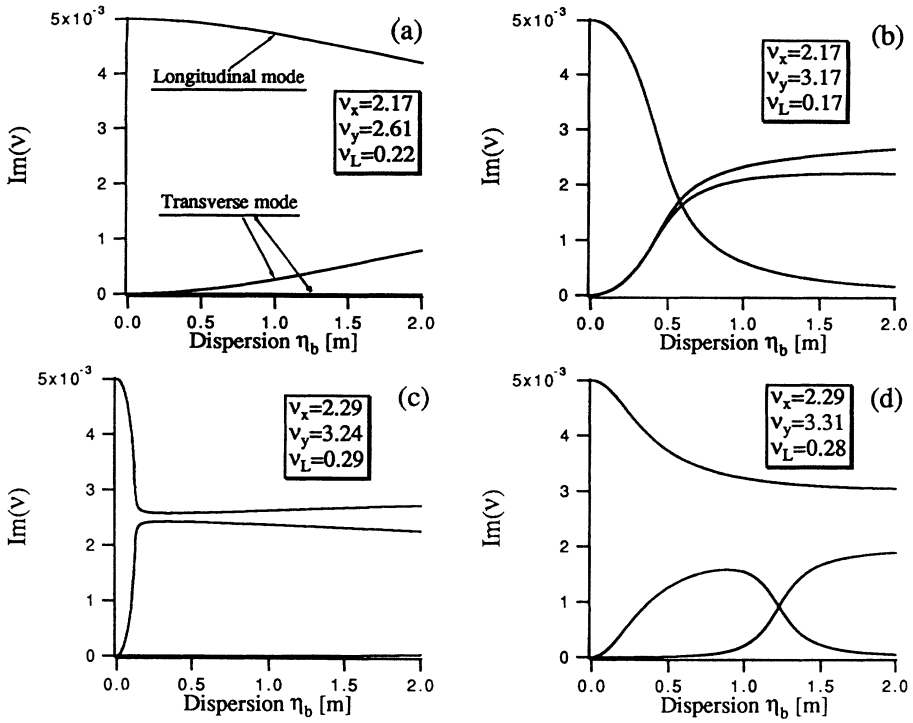

FIG. 3. Imaginary part of the eigentunes evaluated from the 6×6 one-turn transfer matrix vs the dispersion η_b at the cavity position. The origin of the θ coordinate is again taken at the center of the laser cooling section, which has the cooling rate $\Lambda_D/2\pi=0.01$. The RF cavity sits at $\theta_b=\pi$, the position opposite to the cooling section, while the quadrupole location is $\theta_q=3\pi/2$. The quadrupole coupling constant is fixed at $\Gamma_q=0.1$. Only case (b) satisfies the two resonance conditions given in Eqs. (4.3) and (4.12) simultaneously. Note that, in cases (a) and (c), one of the two transverse modes is nearly decoupled, having an imaginary part almost equal to zero.

(4.2) with those in Eqs. (2.12) and (2.13), it is readily recognized that, under the averaging approximation with $\xi_q=0$, the skew-quadrupole potential yields an effect mathematically equivalent to the linearized dispersive coupling at a rf cavity. An enhanced coupling between the horizontal and vertical motions is, therefore, anticipated under the condition

$$\nu_x\left[1-\frac{(\xi_b\nu_L)^2}{\xi_0}\right]^{1/2}-\nu_y=\text{integer}\ , \tag{4.12}$$

which can be approximated as $\nu_x-\nu_y=$ integer. Provided that the resonance conditions in Eqs. (4.3) and (4.12) are satisfied simultaneously, it is actually possible to establish an ideal situation as seen in Fig. 3(b), where the damping-rate curves of the three modes intersect roughly at a single point. The optimum dispersion of the example is $\eta_b\approx0.6$ m.

If one of the two conditions is completely failed, three-dimensional cooling is no longer achievable, as suggested in Fig. 3(c), where Im(ν) of the vertical mode is almost equal to zero. Figure 3(a) shows a situation where both conditions are missed. Needless to say, the damping rates of both transverse modes are too small to accomplish efficient transverse cooling even if the coupling is strengthened. It should also be noted that, in all cases, we do not have a negative damping rate which leads to exponential emittance growth.

Writing $\mu_x=\mu_0$, $\mu_y=\mu_0-2m\pi$, and $\mu_L=\mu_0-2n\pi$ ($m,n=$integer) on the assumption of the two resonance conditions, Eq. (4.11) becomes

$$\left[\lambda+\frac{e^{-\Lambda_D}}{\lambda}-(1+e^{-\Lambda_D})\cos\mu_0\right]\left[\left[\lambda+\frac{1}{\lambda}-2\cos\mu_0\right]^2-\frac{\Gamma_q^2}{\nu_x\nu_y}\sin^2\mu_0\right]$$
$$-\frac{2\pi\nu_x\bar{\nu}_L^2\xi_b^2}{\xi_0}\left[1-\frac{1}{\lambda}\right](\lambda-e^{-\Lambda_D})\sin\mu_0\left[\lambda+\frac{1}{\lambda}-2\cos\mu_0-\frac{\Gamma_q^2(1+\cos\mu_0)}{2\nu_x\nu_y}\right]=0\ . \tag{4.13}$$

Here we have set $\theta_1=\pi$, since, as mentioned in Sec. IV A, this cavity location is most preferable to reduce the required minimum value of the dispersion η_b. We see that the longitudinal mode is nearly decoupled in the region $\xi_b\ll1$, while the two transverse modes almost degenerate. As before, Eq. (4.13) can be approximately solved by treating the term proportional to ξ_b^2 as a perturbation applied to the nonperturbed decoupled motions. After some algebra, the first-order solutions of the transverse damping rates are found to be

$$\text{Im}(\nu)\approx\frac{\nu_x\bar{\nu}_L^2\xi_b^2}{4|\xi_0|}\frac{\tan\dfrac{\mu_0}{2}\pm\dfrac{\Gamma_q}{2\sqrt{\nu_x\nu_y}}}{\left[1\pm\dfrac{\Gamma_q}{\sqrt{\nu_x\nu_y}}\cot\mu_0\right]\tanh\dfrac{\Lambda_D}{2}+\dfrac{\Gamma_q^2}{2\nu_x\nu_y\sinh\Lambda_D}}\ . \tag{4.14}$$

We now have enough information to estimate the optimum dispersion values η_{opt}. It is unnecessary to know the explicit functional form of the longitudinal-mode curve if we notice the fact that the sum of the three damping rates should always be equal to the maximum achievable damping rate $\Lambda_D/4\pi$, the same as the longitudinal one without the coupling. Under the two resonance conditions, the damping-rate curves generally show a property similar to Fig. 3(b); i.e., the curves of two transverse modes grow initially as η_b^2, staying close to each other, and eventually intersect the longitudinal-model curve at roughly the same point. The maximum damping rate is then distributed almost equally to all three modes. Therefore, at the optimum point, the three modes should be given one-third of the maximum rate, namely

$$\mathrm{Im}(\nu_0)=\frac{\Lambda_D}{12\pi} . \tag{4.15}$$

Equating Eqs. (4.14) and (4.15) gives an approximate formula for the optimum dispersion

$$\eta_{opt}^2 \approx \frac{|\xi_0|R^2}{6\pi\nu_x\bar{\nu}_L^2}\left[\Lambda_D^2+\frac{\Gamma_q^2}{\nu_x\nu_y}\right]\cot\frac{\mu_0}{2} , \tag{4.16}$$

where we have dropped some small terms, assuming that $\Lambda_D \ll 1$ and $\Gamma_q/\sqrt{\nu_x\nu_y} \ll 1$. Although the value of η_{opt} predicted by Eq. (4.16) may not always be sufficiently accurate because of the first-order approximation, it permits us to make an initial estimate of the optimum dispersion.

In Fig. 4, we show several examples of damping rates with the parameters simultaneously satisfying the two resonance conditions. The dotted curves are obtained from Eqs. (4.14), while the broken line parallel to the abscissa indicates the level in Eq. (4.15). The validity of Eqs. (4.14), (4.15), and (4.16) has been confirmed beautifully in the present examples.

Equation (4.16) also provides important insight into the parameter dependence of the optimum operating point. In particular, the equation indicates the controllability of η_{opt} by means of the skew-quadrupole strength Γ_q. Thus, even if the actual dispersion deviates from its design value, it is straightforward to recover an optimum operating situation, compensating for the error. All we need in the case is simply to increase or decrease the skew-quadrupole gradient.

V. TRACKING RESULTS

We now show tracking results, confirming the validity of the theoretical predictions given so far. Apart from the laser cooling section, the particle motion governed by the nonlinear Hamiltonian in Eq. (2.2) is simulated in the tracking code employed here. To incorporate the laser cooling effect, the matrix in Eq. (2.11) is used.

Damping rates are related substantially to the product of Λ and θ_D, i.e., Λ_D, rather than Λ itself. The value of Λ_D reflecting actual experimental results cannot be uniquely determined because it strongly depends on the initial state of a stored beam [12]. The fundamental feature of the damping-rate curves in Fig. 4 is, however, not affected even if a different value of Λ_D is chosen. Only the magnitudes of the damping rates are changed, maintaining the similar figures. Thus the value of Λ_D is not essential to how transverse damping rates are enhanced, although cooling time is indeed altered depending on Λ_D. In the present paper, we assume that $\Lambda=0.2$ and $\theta_D/2\pi=0.05$, representing a cooling section of 2-m length.

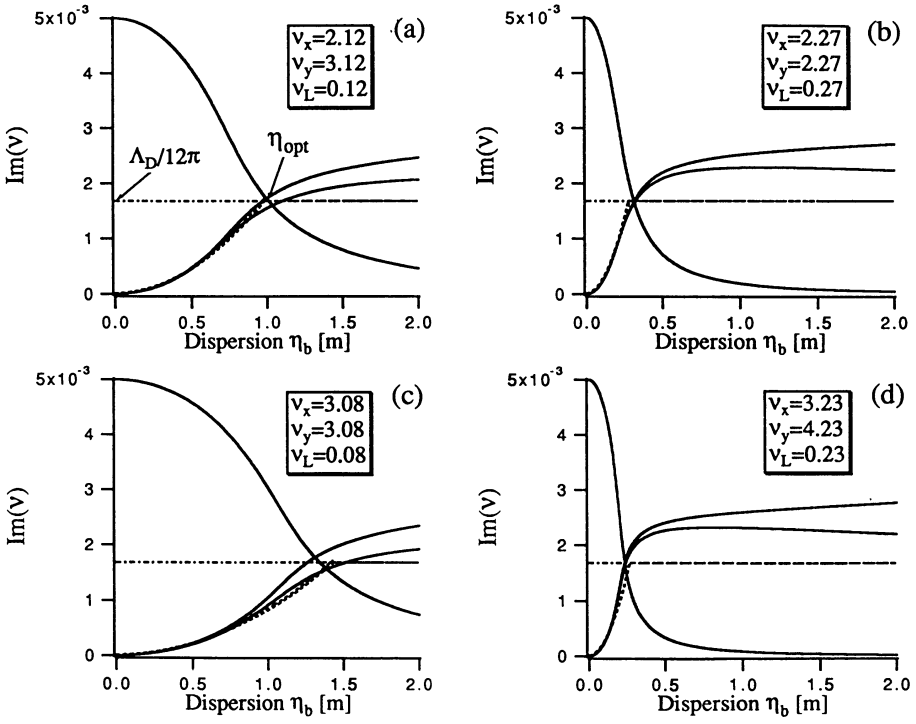

FIG. 4. The same as Fig. 3, but the longitudinal and horizontal tunes here are set at values identical to those adopted in Fig. 2. In addition, the vertical tune is chosen such that the resonance condition $\nu_x-\nu_y$ = integer is satisfied. The dotted curves represent the first-order theoretical solutions given in Eqs. (4.14), yielding close agreements with the numerical results in all cases. It is shown, as expected, that three curves always intersect at the level $\mathrm{Im}(\nu)=\Lambda_D/12\pi$.

First of all, let us consider the parameters adopted in Fig. 3, checking whether the dispersion relation enables us to predict correctly the damping properties of the three motions. The corresponding simulation results are shown in Fig. 5. In all cases, the dispersion η_b is fixed at 0.6 m, which agrees approximately with the optimum value indicated in Fig. 3(b). Equation (4.16) actually gives $\eta_{\text{opt}} \approx 0.57$ m. It is obvious that the results are in accord with the expectations drawn from Fig. 3.

It is practically important to know how much error around the resonance conditions is allowable to keep the damping rates of all three motions sufficiently high. We do not have to pay much attention to dispersion error, since the shift of the optimum operating point due to the error is adjustable with the skew-quadrupole gradient, as pointed out in Sec. IV. As an example, here we investigate the case given in Fig. 4(a), slightly changing the transverse tunes around the values shown. The damping rates are plotted in Fig. 6 as a function of the longitudinal tune ν_L. Specifically, Fig. 6(a) indicates that the optimum ν_L is 0.12. Slight shifts are now applied to the transverse tunes, fixing η_b at 1 m. The deviation $|\nu_x - \nu_y| \leq 0.004$ appears to be permissible to ensure a high level of damping rate for all modes. In the cases in Figs. 6(c) and 6(e), where $|\nu_x - \nu_y| = 0.006$, $\text{Im}(\nu)$ of one mode seems too small, while it still remains positive. These figures also suggest that the rigorous tuning of ν_L is not necessary. The ν_L error of, say, ± 0.002, looks acceptable [13].

The tracking results corresponding to Figs. 6(a)–6(d) are shown in Fig. 7. We observe that even the case in Fig. 7(c) is fine, while the vertical damping is a little slow, as expected. Notice that, in these simulations, initial parameters different from those used in Fig. 5 have been adopted. When assuming a 100-keV $^{24}Mg^+$ ion and the harmonic number $h = 26$, the initial parameters employed represent a beam having a transverse radius of ~ 5 mm, a divergence of ~ 0.8 mrad, and a momentum spread of about $\delta p / p_0 \sim 4 \times 10^{-5}$. These values are even larger than those of the actual beams injected into ASTRID. As for the initial phase spread $\delta\psi$, we have taken $\delta\psi \sim 25°$, but a much larger phase spread is allowable.

Phase-space configurations are illustrated in Fig. 8, starting with the parameters identical to Fig. 7(a) except for a phase spread that is twice as large. The initial emittances of all three directions have been remarkable compressed after 300 turns. It has been confirmed, in additional simulations, that a total phase spread greater than 100° is still acceptable, and that the theoretical predictions based on the present linear approach hold quite valid even for such a beam.

Compared to Fig. 5(b), much more significant initial growths of transverse emittances are observed in Fig. 7. This is due to the larger initial phase spread assumed. Figure 9 demonstrates emittance oscillations when the longitudinal emittance is initially ten times greater than the transverse emittances. Since the operating point must be set on or close to the coupling resonances to enhance transverse cooling rates, a considerable amount of emittance exchange takes place whenever there exists an emittance imbalance. Although a circulating beam is, in principle, stable on a difference resonance, even such a resonance might be avoided between longitudinal and transverse motions in most high-energy synchrotrons, because the longitudinal emittance of an accelerated beam is usually much higher than the transverse emittances and, as a result, a rapid increase of the transverse beam size occurs, leading to a beam loss.

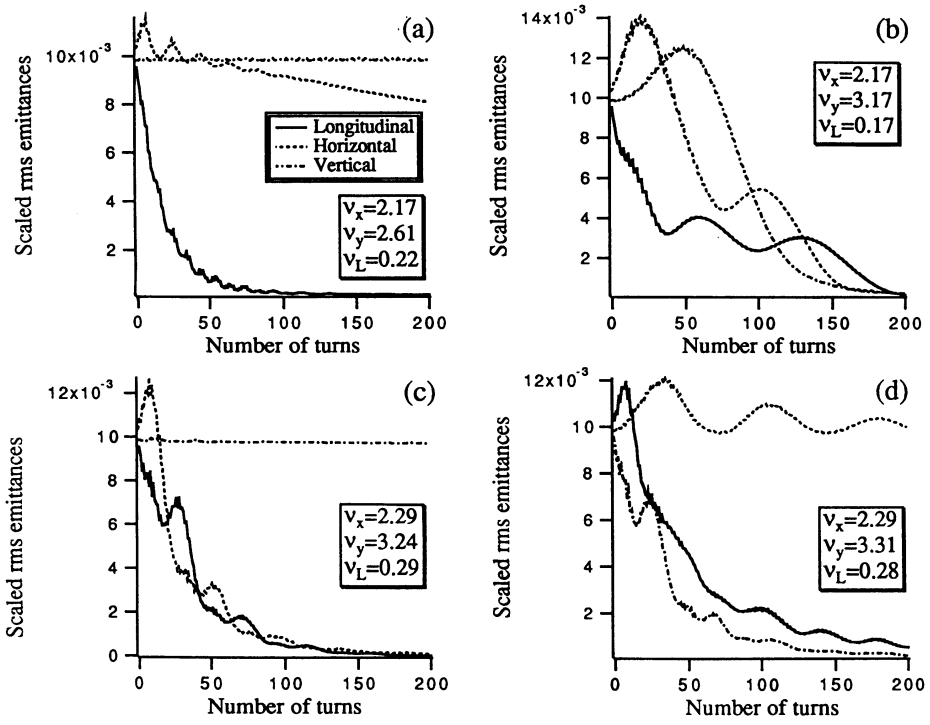

FIG. 5. Tracking results, i.e., the solutions of the nonlinear equations derived from the Hamiltonian in Eq. (2.2), in which 500 particles are followed and, from them, longitudinal (solid line) and transverse (broken lines) rms emittances are evaluated. The employed parameters in each figure are identical to those in Fig. 3, but the dispersion is fixed at $\eta_b = 0.6$ m, approximately corresponding to the optimum value indicated in Fig. 3(b). Initially, particles are randomly distributed inside the three phase-space circles whose scaled radius is 0.1. (See Fig. 8.)

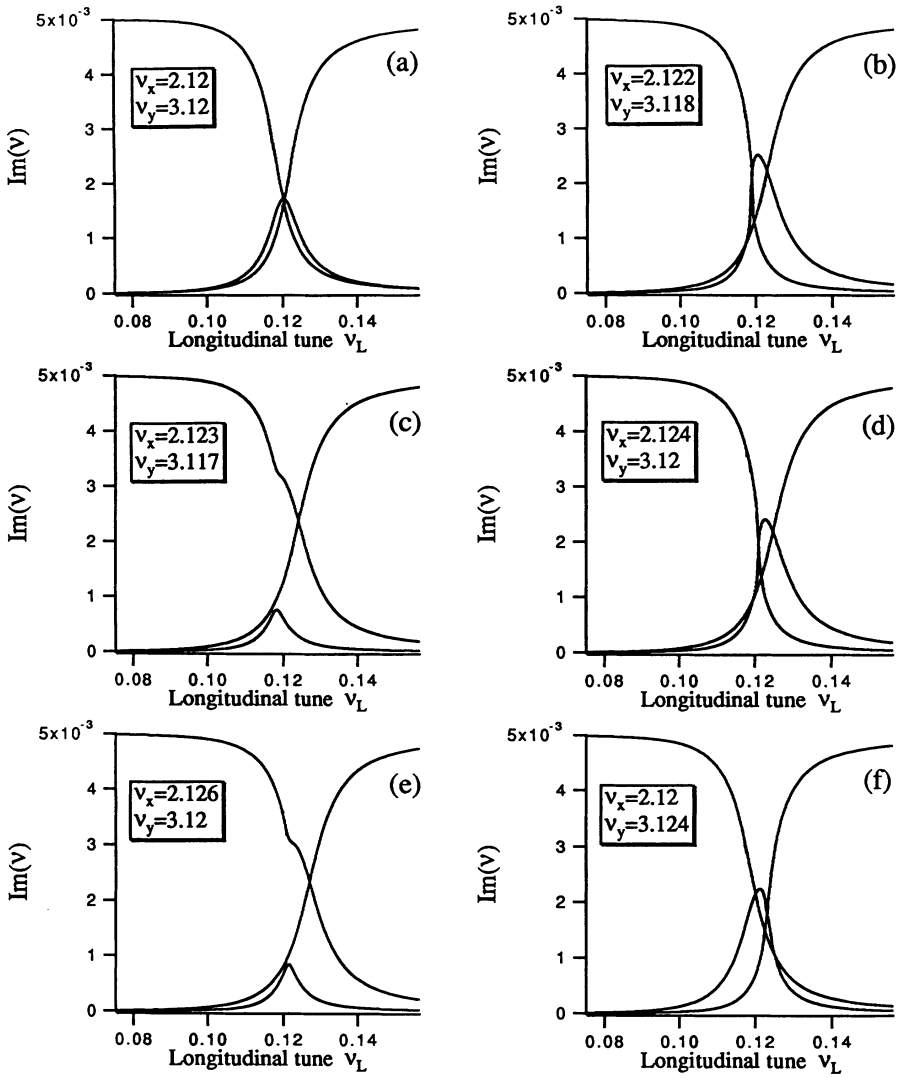

FIG. 6. Imaginary part of the eigentunes evaluated from the 6×6 one-turn transfer matrix vs the longitudinal tune ν_L. The horizontal tune ν_x and the vertical tune ν_y are varied around the values shown in case (a), fixing the dispersion η_b at 1.0 m which is approximately equal to η_{opt}. Other parameters, except for the tunes, are identical to those in Fig. 3. Case (a) represents the best case, where ν_x and ν_y satisfy the resonance condition. Clearly, the optimum situation is achieved when $\nu_L = 0.12$.

In our case, the beam-size growth due to resonant emittance transfer is avoidable simply by precooling the longitudinal temperature with a laser cooler. During the precooling process, the longitudinal tune is set at an off-resonance value by supplying proper rf power to the cavity. Once the beam is bunched and precooled to a longitudinal emittance comparable to the transverse values, we then adjust the tune so as to generate a synchrobetatron resonance for three-dimensional cooling, increasing or decreasing the rf power.

Even if emittance oscillations with large amplitudes arise, as seen in Fig. 9, the emittances, after 400 turns, have reached a level more than 100 times smaller than their initial values. It is interesting to note that the longitudinal emittance always takes its minima around the timing when the sum of the transverse emittances comes to its maxima. This implies the existence of a constant of motion in the absence of the laser-cooling term.

VI. EFFECTS OF ζ_q and $\dot{\zeta}_b$

Here we briefly explore the effects of finite ζ_q and $\dot{\zeta}_b$, neglected so far. Let us first assume a nonzero ζ_q, which is of practical importance because we often have infinite dispersion everywhere along the circumference of a storage ring. In fact, the dispersion functions of both ASTRID and TSR never vanish. Further, provided that the value of ζ_q suitable for three-dimensional cooling is uniquely determined, or strongly dependent upon other ring parameters, a rigorous restriction might be imposed on lattice design. Fortunately, Fig. 10 eliminates this concern. In the figure, the dispersion η_b at the cavity is fixed at 1 m, approximately equal to the optimum value indicated in Fig. 4(a). It is seen that the damping rates are almost unchanged, even if the value of the dispersion $\eta_q \equiv R\zeta_q$ is varied over a wide range.

The effect of $d\eta_b/ds \equiv \dot{\zeta}_b$ is now investigated, neglecting η_q. Figure 11, employing the same parameters as Fig. 4(a), illustrates the η_b dependence of damping rates with various values of the derivative $d\eta_b/ds$. No noticeable change is observed when $d\eta_b/ds$ takes a small value. However, as the derivative becomes larger, the three modes tend to be split up and, eventually, completely spread out as seen in the cases in Figs. 11(c) and 11(d). A large value of $d\eta_b/ds$ must therefore be avoided to make sure of a sufficiently high cooling rate in each mode.

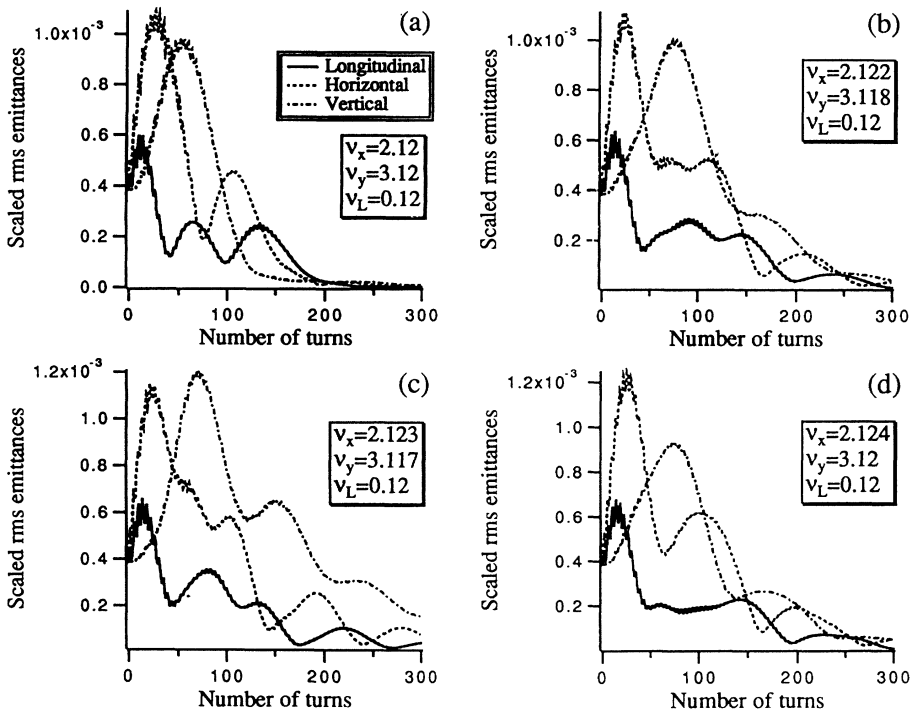

FIG. 7. Tracking results exactly corresponding to cases (a)–(d) given in Fig. 6. The longitudinal tune ν_L is fixed at 0.12. In horizontal and vertical phase spaces, the assumed initial beam has a circular shape with the scaled radius of 0.02, which is $\frac{1}{5}$ of the injection beam radius in Fig. 5. The longitudinal phase-space projection is an ellipse, having a total phase spread of 0.8 radian and a maximum absolute W of 0.001. 500 particles are randomly distributed in the initial state.

It is interesting to note that, apart from constant coefficients, the mathematical roles of ξ_b and ζ_b to the horizontal canonical variables are symmetric, as is clear from the Hamiltonian (2.2). Consequently, plotting $\mathrm{Im}(\nu)$ as a function of the derivative $d\eta_b/ds$, we obtain figures quite similar to Fig. 11. Analogous to the pattern illustrated in Fig. 11, the damping-rate curves are gradually split out with the increasing η_b.

VII. SUMMARY

It has been shown that the dispersion-induced coupling at an rf cavity is a possible way to extend the longitudinal laser cooling effect to transverse degrees of freedom, based on the idea of enhanced synchrobetatron coupling. We have found that the dispersive coupling, under a linear approximation, is mathematically equivalent to the coupling generated by a coupling-cavity potential, but the present scheme has turned out to be more useful when considering practical applications. In fact, the scheme can be applied, without any difficulty, to very low-energy beams, while design of a coupling cavity is not so easy for such a beam. In addition, the previous scheme requires us to provide two different rf cavities; i.e., a coupling cavity operating in the TM_{210} mode, and an ordinary bunching cavity for the purpose of creating an rf bucket. A single ordinary cavity introduced here plays the roles not only of the coupling cavity but also of the bunching cavity. Further, the synchrotron oscillation induced by the cavity field is beneficial to simplifying the laser cooling system. It has been experimentally proven in the ASTRID ring that ions executing synchrotron oscillations can be cooled with only one laser as efficiently as with two lasers, copropagating and counterpropagating with the stored beams [11].

The rf cavity can also be utilized, with a laser cooler turned on, for preventing undesirable nonlinear effects as well as a large amount of emittance transfer from longitudinal to transverse directions. After the precooling process, the longitudinal phase space of an initial continuous beam is compressed, achieving a small emittance with a small phase spread. Consequently, we can make a simple linear regime set in.

Until coming close to an ultracold beam state, the linear analysis described in the paper holds very well. Space-charge force will not affect the present results because the stored beams employed so far for laser cooling experiments have a very low intensity. However, once an ultralow temperature is reached, the beams move into a space-charge-dominated state. Effects of intrabeam scattering and so on, which are generally negligible for a low-intensity beam with a normal temperature, become important [14].

The space-charge-dominated state of a low-intensity ultracold beam may be considered as a first stage toward a crystalline beam. Theoretically, a crystalline beam forms a continuous structure [15], while a laser-cooled beam obtained under the present scheme has been bunched. However, it is an easy matter to debunch the beam, as we have an rf cavity already set on the ring. A procedure to observe a beam crystallization may, therefore, be as follows. First of all, turn on a laser cooling system as well as an rf cavity without the condition in Eq. (4.3) satisfied. After the beam is bunched and longitudinally precooled to some degree, adjust the rf power supplied to the cavity such that the longitudinal tune satisfies the resonance condition. We now also turn on a skew-quadrupole magnet and increase the field strength up to the optimum level theoretically predicted. After a temperature in the mK range is achieved, turn off the laser, and switch the syn-

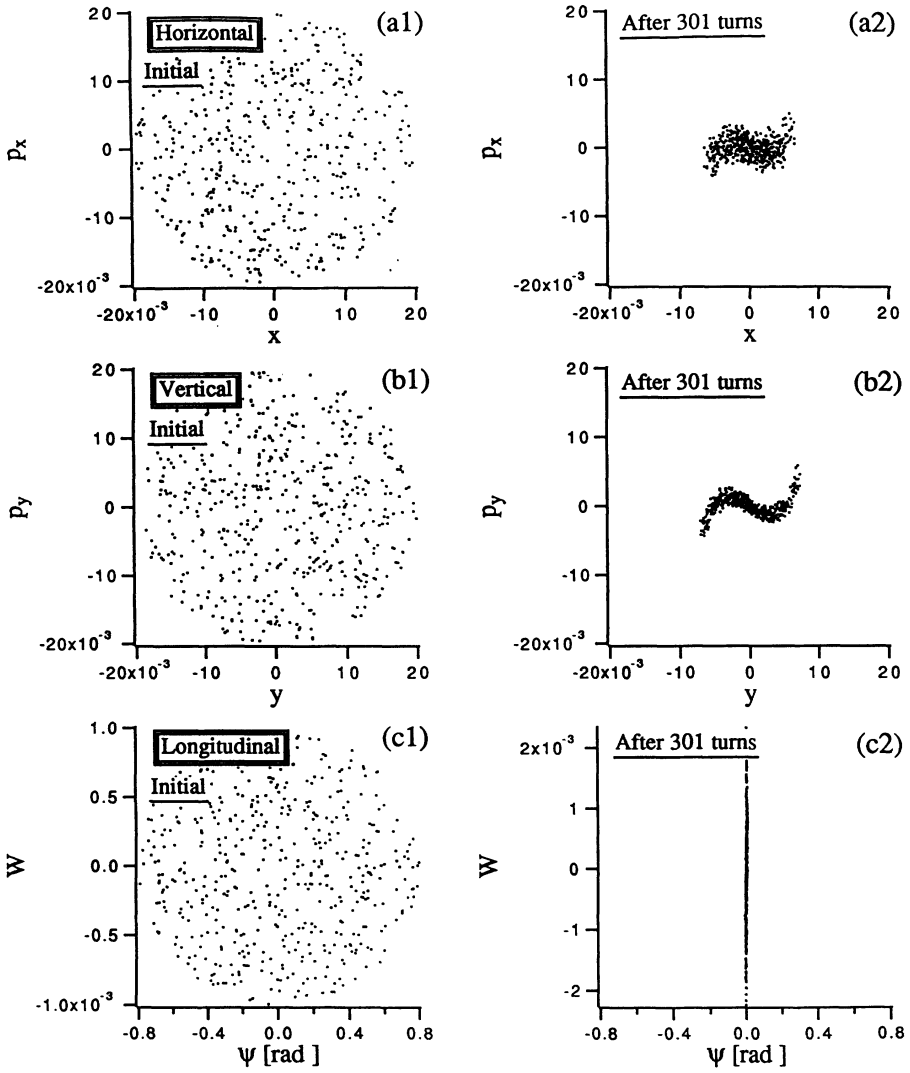

FIG. 8. Phase-space configurations. ($a1$), ($b1$), and ($c1$) represent two-dimensional phase-space projections of an injection beam, while ($a2$), ($b2$), and ($c2$) are those after 301 turns. The parameters employed are exactly the same as those in Fig. 7(a), but the initial phase spread is taken twice as large.

chronous phase to a debunching one. During the debunching process, we may hopefully transform the beam plasma to a liquid state or, eventually, to a crystalline state.

ACKNOWLEDGMENTS

The author would like to thank Dr. A. M. Sessler and Dr. D. Möhl for valuable discussions. He is also indebted to Dr. S. Machida and Dr. K. Hirata for useful conversations, and to Dr. J. S Hangst for kindly providing helpful information of the ASTRID storage ring in Denmark.

APPENDIX A: HAMILTONIAN OF THE SYSTEM

Since the Hamiltonian including effect of an rf cavity has been derived in the previous work [16], here we only outline the derivation for completeness, considering addi-

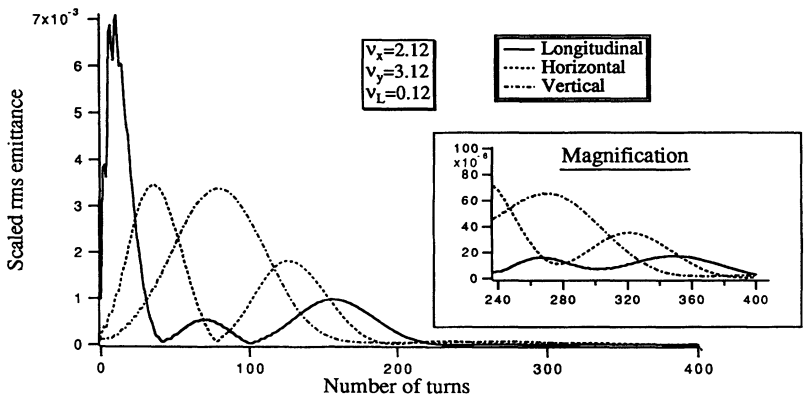

FIG. 9. The same as Fig. 7(a), but here the initial transverse emittance is set at $\frac{1}{4}$ of Fig. 7(a), while the longitudinal emittance is taken to be ten times larger than the transverse value.

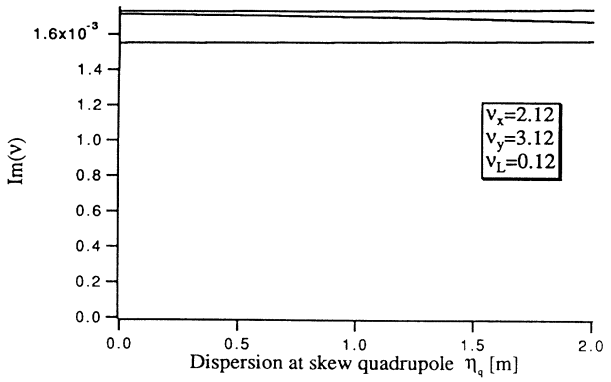

FIG. 10. Dependence of damping rates on the dispersion η_q at the skew quadrupole position. The same parameters as employed in Fig. 4(a) have been assumed fixing the dispersion η_b at 1.0 m.

tionally the potential of pure skew-quadrupole magnets.

Let us consider a storage ring of the average radius R. Our starting point is the general Hamiltonian of the form

$$H_1 = c\left[\frac{(p_s - qA_s)^2}{(1+x/\rho)^2} + (p_x - qA_x)^2 + (p_y - qA_y)^2 + m_0^2 c^2\right]^{1/2}, \tag{A1}$$

where m_0 and q, respectively, are the rest mass and charge state of ions, ρ is the local curvature of the ring, and $\mathbf{A}=(A_x, A_y, A_s)$ represents the total vector potential of the system. We now install rf cavities at the positions $s=s_b^{(n)}$ $(n=1,2,\ldots,N_b)$ and skew quadrupoles at $s=s_q^{(n)}$ $(n=1,2,\ldots,N_q)$, where s is the distance along the reference particle orbit. The vector potential of the nth rf cavity is given by

$$\mathbf{A}_b = \left[0, 0, \frac{V_b^{(n)}}{\omega}\sin(\omega t + \phi_b^{(n)})\right], \tag{A2}$$

where $V_b^{(n)}$ and $\phi_b^{(n)}$ $(n=1,2,\ldots,N_b)$ are, respectively, the voltage amplitude and initial phase of the nth cavity. From a practical point of view, all the cavities have been assumed to be identical, writing the common rf angular frequency as ω. Taking the distance s as the independent variable, instead of time, and considering only dipole and quadrupole magnets installed on the ring, the Hamiltonian H_1 can be approximate, together with Eqs. (A2), as

$$H_2 = -p + (p_0 - p)\frac{x}{\rho} + \frac{p_x^2 + p_y^2}{2p} + \frac{p_0}{2}[K_x(s)x^2 + K_y(s)y^2] + p_0 xy \sum_{n=1}^{N_q} \frac{\Gamma_q^{(n)}}{R}\delta_p(s - s_q^{(n)}) - \frac{q}{\omega}\sum_{n=1}^{N_b} V_b^{(n)}\sin(\omega t + \phi_b^{(n)})\delta_p(s - s_b^{(n)}), \tag{A3}$$

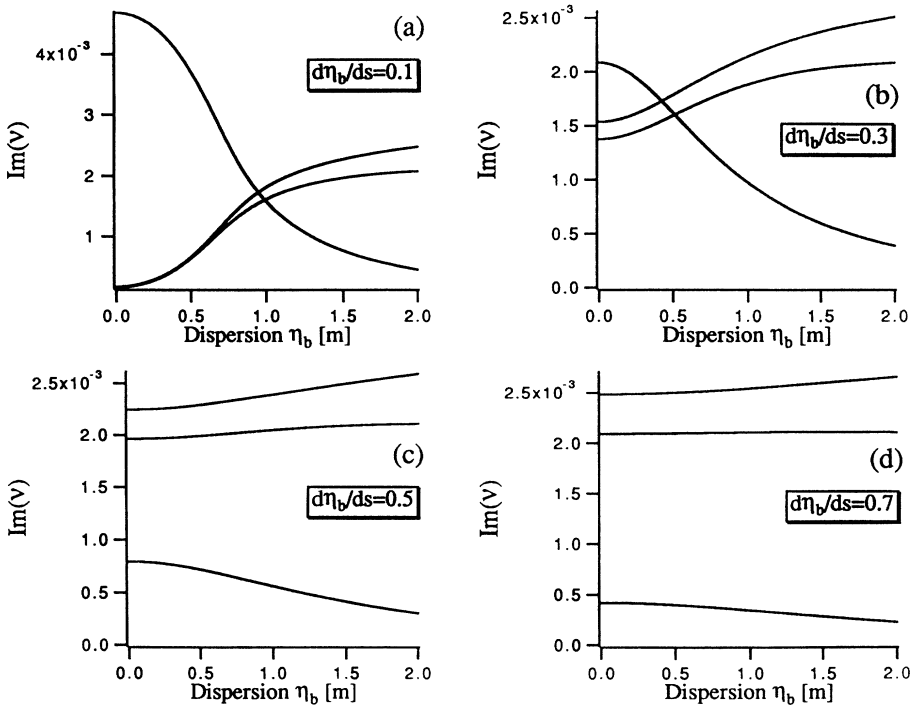

FIG. 11. The same as Fig. 10, but $\mathrm{Im}(\nu)$ is now plotted as a function of the dispersion η_b. Finite values of the dispersion derivative at the cavity position have been assumed, neglecting η_q.

where $\Gamma_q^{(n)}$ is the coupling strength of the nth skew quadrupole, $K_{x(y)}(s)$ is related to the quadrupole filed strength, $\delta_p(s)$ denotes the periodic delta function whose periodicity is the ring circumference $2\pi R$, and the total momentum p is expressed as $p=[(W/c)^2-m_0^2c^2]^{1/2}$ with the total particle energy W. In the following analysis, quantities with the subscript 0 are used to represent those corresponding to the reference particle.

We now introduce the canonical transformation from the variables $(x,y,t;p_x,p_y,-\Delta W=W-W_0;s)$ to $(\tilde{x},\tilde{y},\tilde{t};\tilde{p}_x,\tilde{p}_y,-\Delta\tilde{W};s)$ yielded by the generating function

$$F_1=\tilde{p}_x\left[x-\frac{\eta}{p_0\beta_0c}\Delta\tilde{W}\right]+\tilde{p}_y y + \frac{\eta'}{\beta_0 c}x\Delta\tilde{W}-\frac{\eta\eta'}{2p_0(\beta_0c)^2}(\Delta\tilde{W})^2 , \tag{A4}$$

where $\eta(s)$ is the dispersion function of the ring, β and γ are the usual relativistic parameters, and the prime stands for the derivative with respect to s. After applying this transformation to Eq. (A3), we scale the canonical momenta to obtain

$$H_3=\tfrac{1}{2}(\tilde{p}_x^2+\tilde{p}_y^2)+\tfrac{1}{2}[K_x(s)\tilde{x}^2+K_y(s)\tilde{y}^2]-\frac{\Delta\tilde{W}}{\beta_0c}+\frac{1}{\beta_0c}\left[\frac{1}{\gamma_0^2}-\frac{\eta}{\rho}\right]\frac{(\Delta\tilde{W})^2}{2}+\tilde{y}\left[\tilde{x}+\frac{\eta}{\beta_0c}\Delta\tilde{W}\right]\sum_{n=1}^{N_q}\frac{\Gamma_q^{(n)}}{R}\delta_p(s-s_q^{(n)}) - \frac{q}{p_0\omega}\sum_{n=1}^{N_b}V_b^{(n)}\sin\left[\omega\tilde{t}-\frac{\omega}{\beta_0c}(\eta\tilde{p}_x-\eta'\tilde{x})+\phi_b^{(n)}\right]\delta_p(s-s_b^{(n)}) . \tag{A5}$$

The Hamiltonian H_3 is further transformed with the generating function

$$F_2=\tilde{x}\hat{p}_x+\tilde{y}\hat{p}_y+\left[\omega\left[\tilde{t}-\frac{s-s_b^{(1)}}{\beta_0c}\right]+\phi_b^{(1)}\right]\hat{W} . \tag{A6}$$

The use of F_2 leads to the Hamiltonian

$$H_4=\tfrac{1}{2}(\hat{p}_x^2+\hat{p}_y^2)+\tfrac{1}{2}[K_x(s)\hat{x}^2+K_y(s)\hat{y}^2]-\left[\frac{h}{R}\right]^2\frac{\xi_0\hat{W}^2}{2}+\hat{y}\left[\hat{x}-\frac{h\eta}{R}\hat{W}\right]\sum_{n=1}^{N_q}\frac{\Gamma_q^{(n)}}{R}\delta_p(s-s_q^{(n)}) - \frac{q}{p_0\omega}\sum_{n=1}^{N_b}V_b^{(n)}\sin\left[\hat{\phi}-\frac{h}{R}(\eta\hat{p}_x-\eta'\hat{x})+\Phi_b^{(n)}\right]\delta_p(s-s_b^{(n)}) , \tag{7}$$

where h is the harmonic number of the cavities, ξ_0 is the so-called phase slip factor defined as $\xi_0\equiv\alpha-1/\gamma_0^2$ with the momentum compaction α, and

$$\Phi_b^{(n)}\equiv\frac{h}{R}(s_b^{(n)}-s_b^{(1)})+\phi_b^{(n)}-\phi_b^{(1)} . \tag{A8}$$

APPENDIX B: TRANSFER MATRICES

Here, we give explicit expressions of the transfer matrices employed in the paper. Based on Eqs. (2.3)–(2.8), the transfer matrix at an rf cavity located at a position with nonzero dispersion can be represented as

$$\mathbf{M}_b=\begin{bmatrix} 1+A\xi_b\dot{\xi}_b & -A\xi_b^2 & A\xi_b & 0 \\ A\dot{\xi}_b^2 & 1-A\xi_b\dot{\xi}_b & A\dot{\xi}_b & 0 \\ \multicolumn{2}{c}{\mathbf{0}} & \mathbf{I} & \mathbf{0} \\ 0 & 0 & 1 & 0 \\ A\dot{\xi}_b & -A\xi_b & A & 1 \end{bmatrix} , \tag{B1}$$

where $A\equiv 2\pi\bar{\nu}_L^2/\xi_0$, and $\mathbf{I}$ and $\mathbf{0}$, respectively, denote the 2×2 unit matrix and zero matrix. Similarly, the pure skew-quadrupole matrix $\mathbf{M}_q$ and the drift matrix M_0 can be given as

$$\mathbf{M}_q = \begin{pmatrix} & & 0 & 0 & & \\ & \mathbf{I} & -\Gamma_q & 0 & \mathbf{0} & \\ 0 & 0 & & & 0 & 0 \\ -\Gamma_q & 0 & \mathbf{I} & & 0 & \zeta_q\Gamma_q \\ & & -\zeta_q\Gamma_q & 0 & & \\ & \mathbf{0} & 0 & 0 & \mathbf{I} & \end{pmatrix}, \tag{B2}$$

$$\mathbf{M}_0(\theta_0) = \begin{pmatrix} \cos(\nu_x\theta_0) & \sin(\nu_x\theta_0)/\nu_x & & & & \\ -\nu_x\sin(\nu_x\theta_0) & \cos(\nu_x\theta_0) & & \mathbf{0} & & \mathbf{0} \\ & & \cos(\nu_y\theta_0) & \sin(\nu_y\theta_0)/\nu_y & & \\ & \mathbf{0} & -\nu_y\sin(\nu_y\theta_0) & \cos(\nu_y\theta_0) & & \mathbf{0} \\ & & & & 1 & -\xi_0\theta_0 \\ & \mathbf{0} & & \mathbf{0} & 0 & 1 \end{pmatrix}, \tag{B3}$$

where θ_0 is the angular extent of a drift space. Needless to say, all these matrices are symplectic.

[1] G. I. Budker, At. Energ. **22**, 345 (1967); G. I. Budker, N. S. Dikansky, V. I. Kudelainen, I. N. Meshkov, V. I. Parkhomchuk, A. N. Skrinsky, and B. N. Sukhina, Part. Accel. **7**, 197 (1976).

[2] S. van der Meer, CERN Report No. CERN/ISR-PO/72-31 (1972) (unpublished).

[3] D. J. Wineland and H. Dehmelt, Bull. Am. Phys. Soc. **20**, 637 (1975); T. Hänsch and A. Schawlow, Opt. Commun. **13**, 68 (1975).

[4] S. Schröder, R. Klein, N. Boos, M. Gerhard, R. Grieser, G. Huber, A. Karafillidis, M. Krieg, N. Schmidt, T. Kühl, R. Neumann, V. Balykin, M. Grieser, D. Habs, E. Jaeschke, D. Krämer, M. Kristensen, M. Music, W. Petrich, D. Schwalm, P. Sigray, M. Steck, B. Wanner, and A. Wolf, Phys. Rev. Lett. **64**, 2901 (1990).

[5] J. S. Hangst, M. Kristensen, J. S. Nielsen, O. Poulsen, J. P. Schiffer, and P. Shi, Phys. Rev. Lett. **67**, 1238 (1991).

[6] H. Okamoto, A. M. Sessler, and D. Möhl, Phys. Rev. Lett. **72**, 3977 (1994).

[7] J. S. Hangst, K. Berg-Sørensen, P. S. Jessen, M. Kristensen, K. Mølmer, J. S. Nielsen, O. Poulsen, J. P. Schiffer, and P. Shi, Nucl. Instrum. Methods B **68**, 17 (1992).

[8] J. P. Schiffer and P. Kienle, Z. Phys. A **321**, 181 (1985).

[9] In the coupling-cavity scheme [6], an rf bunching cavity, as well as a coupling cavity, must be introduced to obtain synchrotron oscillations.

[10] For example, in the storage ring ASTRID, the transverse rms radius of a stored beam is around 3 mm. Assuming the harmonic number $h=26$ for the cavity, the same as employed in the ring to bunch a 100-keV $^{24}Mg^+$ beam, $\zeta_b x$ becomes less than 0.025 under the scaling performed even when $d\eta/ds \sim 2$ at the cavity position. (In ASTRID, the maximum $d\eta/ds$ is 1.71.) Similarly, $\zeta_b p_x$ is estimated as ~ 0.004 for $\eta \sim 2$ m.

[11] J. S. Hangst, J. S. Nielsen, O. Poulsen, J. P. Schiffer, P. Shi, and B. Wanner (unpublished).

[12] J. S. Hangst (private communication).

[13] Assuming the parameters employed for the recent experiments on ASTRID, i.e., $h=26$ and a 100-keV $^{24}Mg^+$-ion beam, the ν_L error of ± 0.002 around the optimum value $\nu_L = 0.12$, corresponds to the rf-voltage error of ± 22.4 V, while only 700 V is enough to achieve $\nu_L = 0.12$. Thus a voltage error of $\pm 3\%$ is permissible in the present example.

[14] H. J. Miesner, M. Grieser, R. Grimm, A. Gruber, D. Habs, W. Petrich, D. Schwalm, B. Wanner, and H. Wernøe (unpublished).

[15] J. Wei, X.-P. Li, and A. M. Sessler (unpublished); Brookhaven National Laboratory Report No. BNL-52381, Upton, New York (1993) (unpublished).

[16] See, for example, C. J. A. Corsten and H. L. Hagedoorn, Nucl. Instrum. Methods A **212**, 37 (1983); T. Suzuki, Part. Accel. **12**, 237 (1982).